



## Article

# Optical Characterization of ALD-Coated Nanoporous Alumina Structures: Effect of Sample Geometry or Coated Layer Material

Ana Laura Cuevas <sup>1</sup>, Víctor Vega <sup>2</sup>, Antonia Domínguez <sup>1</sup>, Ana Silvia González <sup>3</sup>, Víctor M. Prida <sup>3,\*</sup>  
and Juana Benavente <sup>4,\*</sup>

<sup>1</sup> Unidad de Nanotecnología, SCBI Centro, Universidad de Málaga, E-29071 Málaga, Spain

<sup>2</sup> Laboratorio de Membranas Nanoporosas, Servicios Científico-Técnicos, Universidad de Oviedo, E-33006 Oviedo, Spain

<sup>3</sup> Departamento de Física, Facultad de Ciencias, Universidad de Oviedo, E-33007 Oviedo, Spain

<sup>4</sup> Departamento de Física Aplicada I, Facultad de Ciencias, Universidad de Málaga, E-29071 Málaga, Spain

\* Correspondence: vmpp@uniovi.es (V.M.P.); j\_benavente@uma.es (J.B.)

**Abstract:** Optical characterization of nanoporous alumina-based structures (NPA-bSs), obtained by ALD deposition of a thin conformal SiO<sub>2</sub> layer on two alumina nanosupports with different geometrical parameters (pore size and interpore distance), was performed by two noninvasive and nondestructive techniques such as spectroscopic ellipsometry (SE) and photoluminescence (Ph) spectra. SE measurements allow us to estimate the refraction index and extinction coefficient for the studied samples and their dependence with wavelength for the 250–1700 nm interval, showing the effect of sample geometry and cover-layer material (SiO<sub>2</sub>, TiO<sub>2</sub>, or Fe<sub>2</sub>O<sub>3</sub>), which significantly affect the oscillatory character of both parameters, as well as changes associated with the light incidence angle, which are attributed to surface impurities and inhomogeneity. Photoluminescence curves exhibit a similar shape independently of sample pore-size/porosity, but they seem to affect intensity values. This analysis shows the potential application of these NPA-bSs platforms to nanophotonics, optical sensing, or biosensing.

**Keywords:** nanoporous alumina structures; ellipsometric spectroscopy; atomic layer deposition; photoluminescence; optical properties



**Citation:** Cuevas, A.L.; Vega, V.; Domínguez, A.; González, A.S.; Prida, V.M.; Benavente, J. Optical Characterization of ALD-Coated Nanoporous Alumina Structures: Effect of Sample Geometry or Coated Layer Material. *Micromachines* **2023**, *14*, 839. <https://doi.org/10.3390/mi14040839>

Academic Editor: Andrey V. Novitsky

Received: 6 March 2023

Revised: 29 March 2023

Accepted: 1 April 2023

Published: 12 April 2023



**Copyright:** © 2023 by the authors. Licensee MDPI, Basel, Switzerland. This article is an open access article distributed under the terms and conditions of the Creative Commons Attribution (CC BY) license (<https://creativecommons.org/licenses/by/4.0/>).

## 1. Introduction

Atomic layer deposition (ALD), also known as atomic layer epitaxy, is a nanofabrication technique especially suited to grow thin film coatings onto complex substrates. Furthermore, as a consequence of its self-limiting deposition nature, ALD displays other remarkable features that are unique to this technique, such as atomic control on the thickness of the deposited layers and the possibility of growing nanolaminates or stacks of different material layers [1–3]. Therefore, ALD is usually considered a promising technique with huge prospects in the fields of micro- and nanofabrication technologies [3–5]. In addition to that, the combined use of ALD with either soft or hard templates opens up a new route for the development of novel nanomaterials and nanodevices through the so-called atomic layer assembly fabrication method [6–8]. These advanced nanomaterials have found promising applications in fields such as catalysis [9–11], energy conversion and storage [12–19], or photonics [7,8,20]. For these applications, the precise control of the deposited materials thickness and composition, which can be achieved by atomic layer deposition techniques, becomes a key enabling factor.

On the other hand, nanoporous alumina structures (NPASs) obtained by electrochemical anodization of aluminum foils using the two-step anodization method [21,22] are nowadays systems of great interest due to their structural regularity (cylindrical nanopores without tortuosity and very narrow pore size distribution) and large specific surface area [23,24]. A significant characteristic of this fabrication process is the easy modification

of NPAS geometrical parameters by simple variation of the anodization conditions used during the first step (electrolyte solution, applied voltage, and/or temperature), which allows samples with average pore sizes ranging between 20 and 400 nm and an interpore distance between 40 and 450 to be obtained [25,26]. NPASs were initially used in the fabrication of nanorows, nanowires, and membranes for separation of heavy metal cations and drug delivery due also to their good chemical/thermal stability and hardness, although lately they have also been considered for catalysis, optoelectronics, and sensing applications [26–30], but the photonic crystal character associated with their regular nanostructure was already reported [31,32]. In this context, the effect of sample porosity and pore size on optical characteristic parameters such as refraction index, extinction coefficient, and/or dielectric constant has also been considered lately [33,34]. Other characteristics such as photoluminescence or solar absorptivity have also been reported, opening the use of NPASs as sensors, light-emitting diodes, and solar cells [35–38]. In this context, as it was already reported [39–41], surface coating of the NPASs by one or two layers of different ceramic oxides ( $\text{SiO}_2$ ,  $\text{Fe}_2\text{O}_3$ ,  $\text{TiO}_2$ ,  $\text{ZnO}$ , ...) by the ALD technique has permitted the modification of the geometrical, ionic transport, and optical parameters of these nanoporous alumina-based structures (NPA-bSs). On the other hand, both electrochemical anodization and ALD coating processes might provoke the presence of impurities on sample surfaces as well as the increase of its roughness (coalescent effect associated with cover layer formation [42]), which can have an influence on the values of different optical parameters of these NPA-bSs, and consequently, information related to such effects is necessary. Another point of interest is the influence of the ALD coating layer on the photoluminescence character of the NPASs, which seems to depend on several factors that are related to sample fabrication and affect the pore size/porosity of the samples [43], since it could be useful in some applications of NPA-bSs (sensing and biosensing systems [44]).

Different techniques can be used for the optical characterization of thin films [45–47], with spectroscopy ellipsometry (SE) measurements being one of the most surface-sensitive optical tools for the characterization of substrates and overlayers used for different sensor applications [48–50]. SE is a precise and accurate surface technique for characterizing substrates and overlayers, commonly used for the determination of basic optical parameters of thin films such as the refractive index ( $n$ ) and the extinction coefficient ( $k$ ), two parameters related to the interaction between materials and incident light and associated with refraction or absorption, respectively, as well as the dielectric constant (real ( $\epsilon_r$ ) and imaginary ( $\epsilon_i$ ) parts). The knowledge of optical constants provides the fundamental basis for designing and manufacturing optical devices, but morphological/structural (layer thickness or roughness) information can also be obtained by modeled analysis of the SE data [51,52]. In this context, SE is nowadays commonly used for the characterization of coatings in different fields (materials protection, photovoltaic materials, flat panel display devices, biological layers, biofilms, etc.) [53,54].

In this work, the effect of geometrical characteristics (pore size and porosity) on the optical behavior of two NPA-bSs samples, obtained by coating them with a  $\text{SiO}_2$  layer (by the ALD process), two NPASs with different geometrical parameters, are analyzed. As it is well known, silicon dioxide is a remarkably interesting material for surface modification due to its high chemical and thermal stability as well as its dielectric nature, and ALD of  $\text{SiO}_2$  layers offers exceptional deposition conformality for nanoporous alumina structures with a high aspect ratio [55]. Optical characterization was performed by: (i) spectroscopic ellipsometry (SE) measurements at three different light incident angles for wavelengths covering the visible and near infrared (NIR) optical regions; and (ii) photoluminescence spectra with a 325 nm excitation laser. Moreover, the effect of surface material on refractive index and extinction coefficient values as well as on the photoluminescence character of the samples was also considered by comparing the results obtained for the  $\text{SiO}_2$ -covered sample with those for other NPA-bSs with similar pore size and porosity but different ALD coating layers ( $\text{TiO}_2$  or  $\text{Fe}_2\text{O}_3$ ). The results obtained can be of interest for optical applications of nanoporous ceramic samples.

## 2. Materials and Methods

### 2.1. Materials

Aluminum discs (0.5 mm in thickness and 25 mm in diameter) of high purity (Al 99.999%, Goodfellow, UK), previously cleaned with isopropanol and ethanol and electropolished in a 1:3 vol. solution of perchloric acid in ethanol, were employed as substrates for the fabrication of NPA-bSs samples by the two-step anodization process. The anodization process employed a solution of oxalic acid (0.3 M) as the electrolyte and 40 V for the anodization voltage [21,22,56], and the first anodization step was performed during 24 h at 0–1 °C; after this process, an acidic solution of CrO<sub>3</sub> and H<sub>3</sub>PO<sub>4</sub> at 35 °C for 24 h was used for removing the aluminum oxide layer. Then, the second anodization step, under the same anodization conditions, was carried out by adjusting the time until the NPAS achieved a thickness of ~60 μm; an aqueous mixture of HCl and CuCl<sub>2</sub> was employed in order to remove an area of around 1 cm<sup>2</sup> of the remaining Al at the NPAS's underside. Furthermore, we employed H<sub>3</sub>PO<sub>4</sub> 5% aqueous solution at room temperature to remove the alumina barrier layer that blocks the pores bottom. The time for this wet chemical etching was 90 min. Finally, we carried out a widening of the pores through chemical etching in an H<sub>3</sub>PO<sub>4</sub> 5% aqueous solution at 30 °C in order to adjust the initial pore diameter of 35 nm to the desired value for the specific samples.

Once we have synthesized the NPASs, ALD coating of the samples was performed in a Savannah 100 thermal ALD reactor (Cambridge Nanotech, Waltham, MA, USA), using exposure mode, in which the gaseous precursors are let stay in the reaction chamber for prolonged times, thus allowing them to diffuse along the high aspect ratio pore channels of NPAS. Different precursors (3-Aminopropyl)triethoxysilane, titanium tetraisopropoxide, and ferrocene), were used for the deposition of the different conformal coating layers (SiO<sub>2</sub>, TiO<sub>2</sub>, and Fe<sub>2</sub>O<sub>3</sub>, respectively) [40,41], and Ar was also used as a purge and carrier gas. Furthermore, we employed different oxidant agents (O<sub>3</sub> or H<sub>2</sub>O), depending on the specific chemistry of the ALD precursor used for the functionalization of the NPA-bSs. The time and temperature were different depending on the precursor employed in the ALD processes for the different coating materials. The selected precursor temperature, pulse time durations, and experimental conditions are indicated in Table 1. For all processes, an Ar flow of 50 sccm was selected between two subsequent precursor pulses during 90 s in order to remove the excess reactants and resulting by-products of the ALD process. Finally, we had to take into account the different growth rates of each metal oxide, and we accordingly selected the number of ALD cycles for the different processes to adjust the thickness of the deposited layer to around 4–5 nm [57].

**Table 1.** Times and temperatures employed in the ALD processes for the different coating materials, where  $t_1$  is the precursor pulse time;  $t_2$  is the exposition time; and  $t_3$  is the purge lapse. For each material, the times used in the exposure to each precursor are shown by columns, whereas the precursor and substrate temperatures are indicated by lines.

Material (Substrate Temperature)	Precursors (Precursor Temperature)	$t_1$ (s)	$t_2$ (s)	$t_3$ (s)
SiO <sub>2</sub> (150 °C)	H <sub>2</sub> O (60 °C)	1	60	120
	O <sub>3</sub> (25 °C)	0.1	60	120
	H <sub>2</sub> N(CH <sub>2</sub> ) <sub>3</sub> Si(OC <sub>2</sub> H <sub>5</sub> ) <sub>3</sub> (100 °C)	2	60	120
TiO <sub>2</sub> (200 °C)	H <sub>2</sub> O (60 °C)	1	60	120
	Ti[OCH(CH <sub>3</sub> ) <sub>2</sub> ] <sub>4</sub> (75 °C)	1	60	60
Fe <sub>2</sub> O <sub>3</sub> (230 °C)	O <sub>3</sub> (25 °C)	0.1	60	120
	C <sub>10</sub> H <sub>10</sub> Fe (100 °C)	3	60	120

## 2.2. Surface Analysis

Scanning electron microscopy (SEM) images of the top view of the different NPA-bSs studied in this work were obtained in a tungsten-filament SEM (JEOL-5600 Akishima, Tokyo, Japan) operated at 20 kV. Due to the electrically isolating character of the NPA-bSs, the samples were sputtered with a thin conductive gold layer. Image analysis was employed to extract the average values of pore diameter, interpore distance, and porosity from the SEM images, using for that purpose ImageJ (v 1.53t) software [58].

## 2.3. Optical Characterizations

Spectroscopic Ellipsometry (SE) measurements were carried out for wavelengths ranging between 250 nm and 1700 nm with unsupported samples using a goniometer spectrometer (Sopra-Semilab GES-5E, Paris, France), which allows the automatic selection of measurements angles; three different angles (65°, 70°, and 75°) were selected. WinElli software from Sopra-Semilab (Paris, France) was used for data analysis and fittings.

Spectroscopic ellipsometry is a contactless technique used to characterize single layers, or a small number of well-defined layers, as optically homogeneous and isotropic. SE measures the change in the polarization state of light after reflection from a sample surface through the so-called ellipsometric angles,  $\psi$  and  $\Delta$ , related to the amount of reflected light polarized in the perpendicular plane with respect to the incidence light plane ( $r_p$ ) and the amount of reflected light polarized in a plane parallel to the incidence light plane ( $r_s$ ), as it is schematically indicated in Figure 1a. These parameters are related by the following expression [51,59–61]:

$$\tan(\Psi) \cdot e^{i\Delta} = r_p / r_s \quad (1)$$

where  $\tan(\Psi)$  is the amplitude ratio upon reflection and  $\Delta$  is the phase shift difference [61]. Figure 1b shows the scheme of light reflection for a two-layer sample.

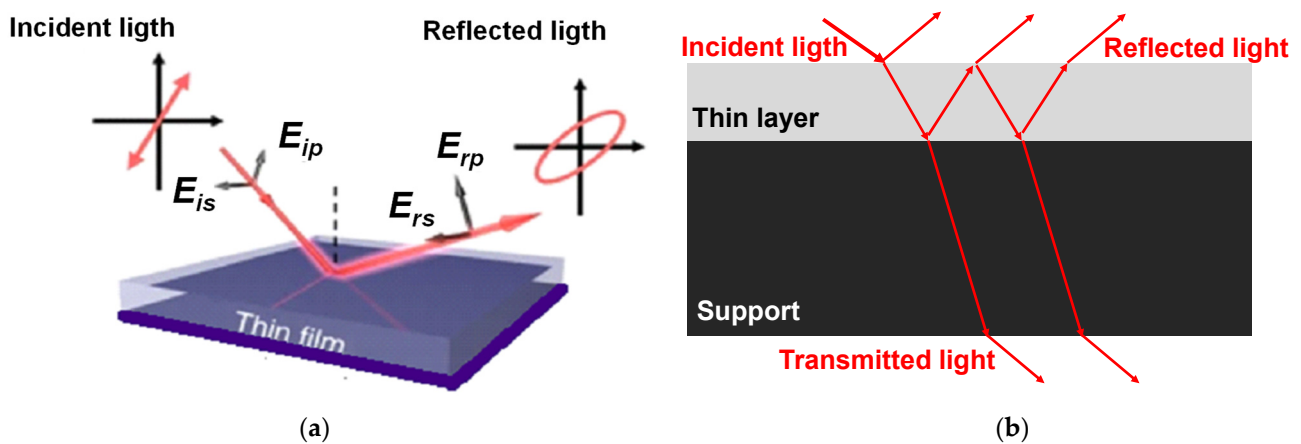


**Figure 1.** Scheme of: (a) polarization states of incident light and after reflection from a surface; (b) incident, reflected, and transmitted light for a supported thin layer.

The Photoluminescence (PL) character of the studied samples was measured with a photoluminescence microscope from HORIBA Scientific (LabRam PL Microscope, Kyoto, Japan), at room temperature, using a 325 nm laser as an excitation light source with a beam power of 0.2 mW in the range from 325 to 700 nm.

## 3. Results and Discussion

### 3.1. SEM Characterization

Figure 2 displays SEM micrographs of the top surfaces of both NPASs and NPAS/SiO<sub>2</sub> samples, showing a high ordering degree of the nanopore arrangement and their nearly non-disperse pore size distribution. From these images, pore diameter values were obtained through computer-assisted image analysis [58]. The images in Figure 2a,b correspond to

samples of Ox(A) before and after applying a SiO<sub>2</sub> coating by ALD (Ox(A)/SiO<sub>2</sub> sample), evidencing a reduction in the average value of pore diameter from 34 to 22 nm, which corresponds to the thickness of the ALD SiO<sub>2</sub> layer deposited into the pores of the nanoporous alumina membrane. A similar percentage reduction in pore diameter after pores were covered with a SiO<sub>2</sub> layer can be observed for samples Ox(B) (53 nm diameter) and Ox(B)/SiO<sub>2</sub> (42 nm pore diameter) in Figure 2c and d, respectively, thus evidencing the reliability and conformality of SiO<sub>2</sub> layers deposited by ALD.

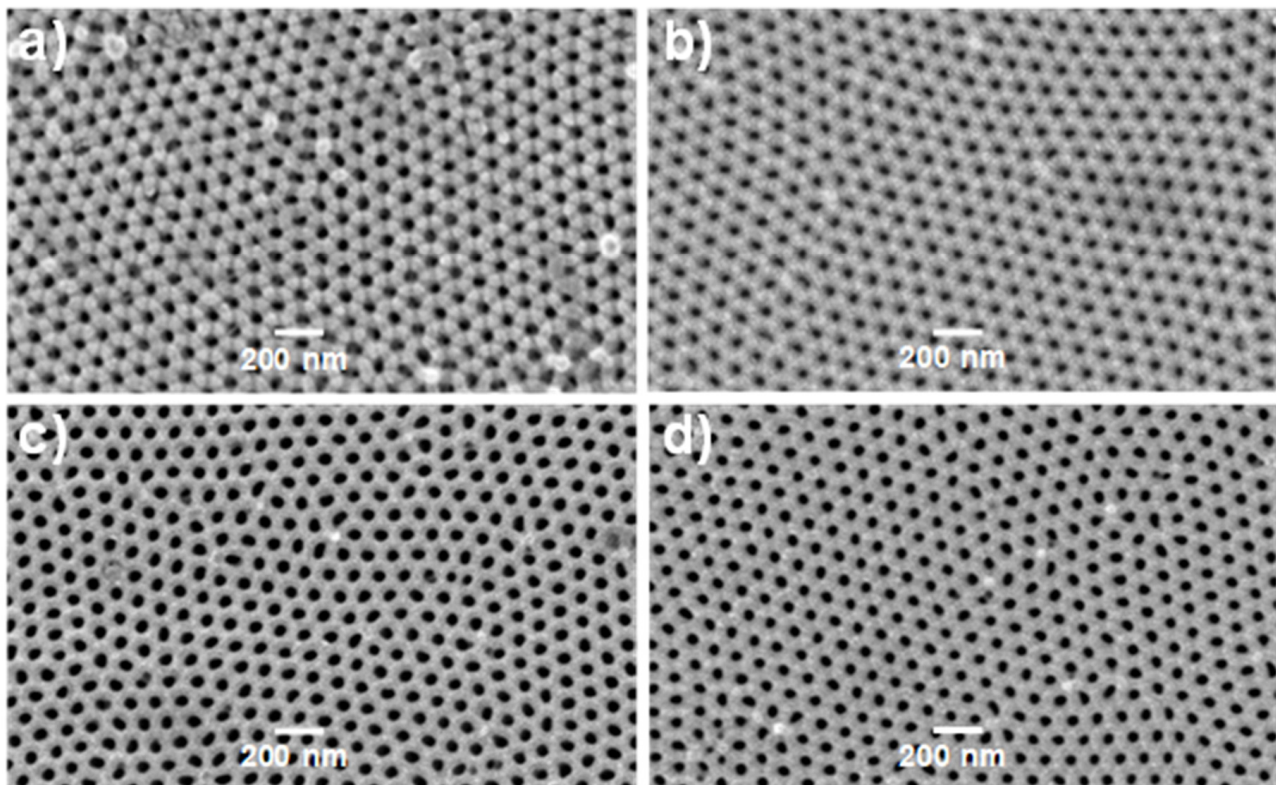


**Figure 2.** SEM top surface images of samples (a) Ox(A), (b) Ox(A)/SiO<sub>2</sub>, (c) Ox(B), and (d) Ox(B)/SiO<sub>2</sub>.

### 3.2. Optical Characterization

Optical techniques for the characterization of thin films, such as spectroscopic ellipsometry (SE) or photoluminescence (Ph), are of great importance since they are non-destructive measurements and do not need vacuum environments, and they provide significant information on important parameters or characteristics of the analyzed samples. In addition to the use of SE for the estimation of thin samples thickness, information on superficial modifications (impurities and/or roughness [62,63]) is also of interest since it could affect optical parameters.

Figure 3 shows a comparison of wavelength dependence for both SE experimental parameters,  $\tan(\Psi)$  and  $\cos(\Delta)$ , for the two studied samples (Ox(A)/SiO<sub>2</sub> and Ox(B)/SiO<sub>2</sub>) at three light incident angles ( $\phi_0 = 65^\circ, 70^\circ$ , or  $75^\circ$ ), where differences depending on both sample geometry (pore-size/porosity) and incident angle can be observed. The main differences between both samples in the results shown in Figure 3 are the high number of oscillations exhibited by  $\cos(\Delta)$  for the Ox(A)/SiO<sub>2</sub> sample in both visible and NIF regions, independently of incident angle, while only small differences between both samples were obtained for  $\tan(\Psi)$  values. However, it should be indicated that recorded values for the Ox(B)/SiO<sub>2</sub> sample present very high dispersion for wavelengths higher than 1000 nm, and smoothed values for the 1000–1700 nm interval are indicated in Figure 3c,d, which could be related to the high transmittance of the sample for such a wavelength interval, but

recorded values (without any manipulation) are presented as Supplementary Information (Figure S1).

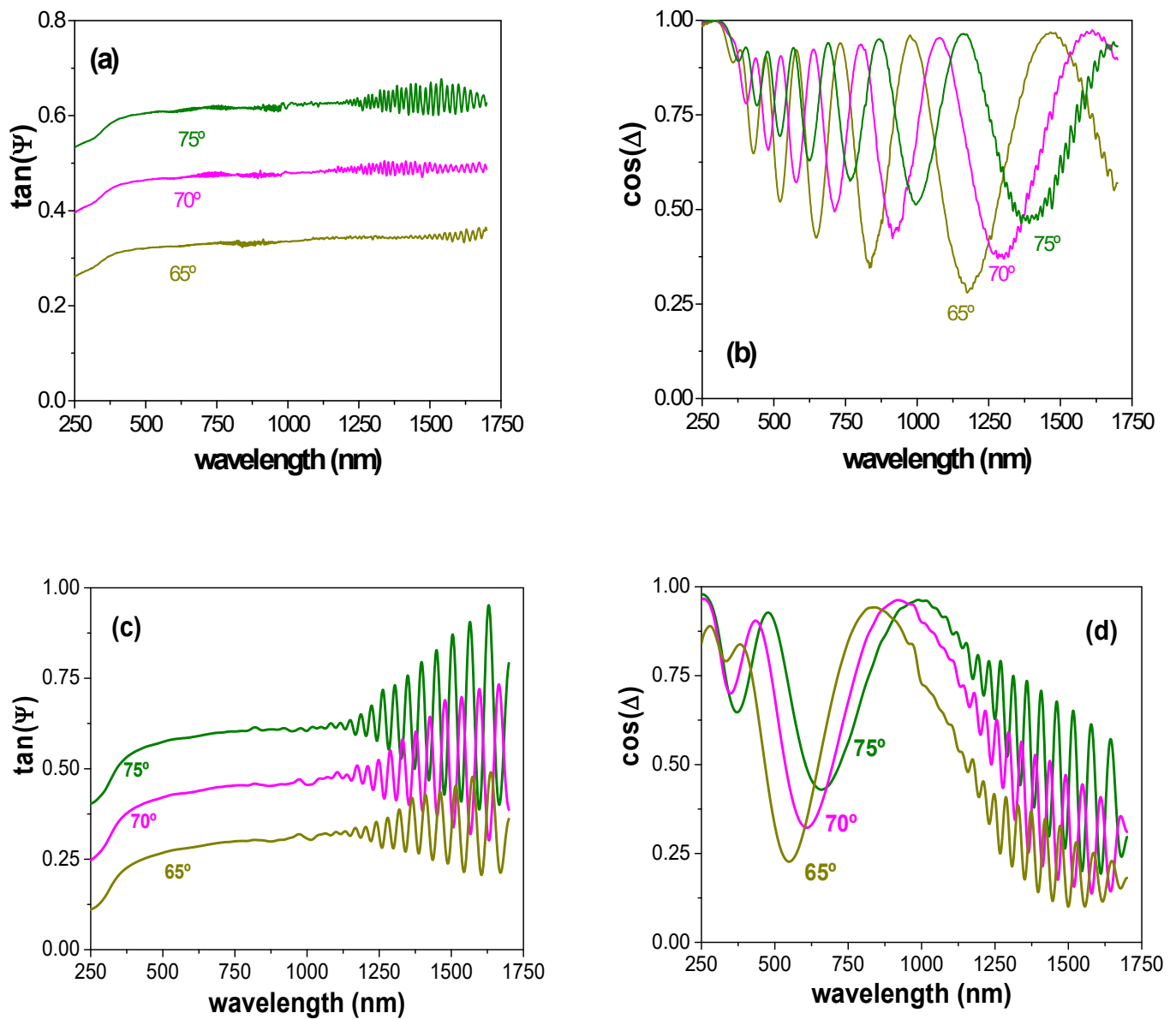


**Figure 3.** Wavelength dependence for  $\tan(\Psi)$  and  $\cos(\Delta)$  at three light incident angles: 65° (dark yellow lines), 70° (magenta lines), and 75° (green lines). (a,b): Ox(A)/SiO<sub>2</sub> sample; (c,d): Ox(B)/SiO<sub>2</sub> sample.

Optical characteristic parameters such as the refractive index ( $n$ ) and the extinction coefficient ( $k$ ) can be determined from SE measurements using the ellipsometer software, and wavelength dependence for sample Ox(A)/SiO<sub>2</sub> at the three light incident angles is shown in Figure 4a,b, respectively, while the variation of  $n$  and  $k$  with wavelength for the Ox(B)/SiO<sub>2</sub> sample is shown in Figure 4c,d. As it can be observed, both samples exhibit wavelength oscillations, a characteristic of photonic crystals, with that effect being more significant for the Ox(A)/SiO<sub>2</sub> sample, in agreement with its lower pore radii according to previous results [34]. This oscillatory behavior found in semiconducting and dielectric thin films has been theoretically modeled by Bao and Xu [64], although the complex morphology of NPA-bSs makes it difficult to apply to our system. On the other hand, a reduction in the values of the refractive index with the increase of the incident angle was obtained, which is attributed to the inhomogeneity and impurity of the top layer of the samples [41,65]. This latter point was already established by depth profile X-ray photoelectron spectroscopy

(XPS) analysis (a destructive technique) [40,41], and it is mainly associated with the coating layer process (use of  $\text{H}_2\text{N}(\text{CH}_2)_3\text{Si}(\text{OC}_2\text{H}_5)_3$  as a precursor for these samples), since those results indicate a high atomic concentration percentage of carbon on the sample surface and its reduction by around 50% after 0.6 sec of argon etching. In this context, the variation of the atomic concentration percentages of the different elements detected on the surface of an  $\text{Ox}/\text{SiO}_2$  sample with the XPS sputtering time is presented as Supplementary Information (Figure S2).

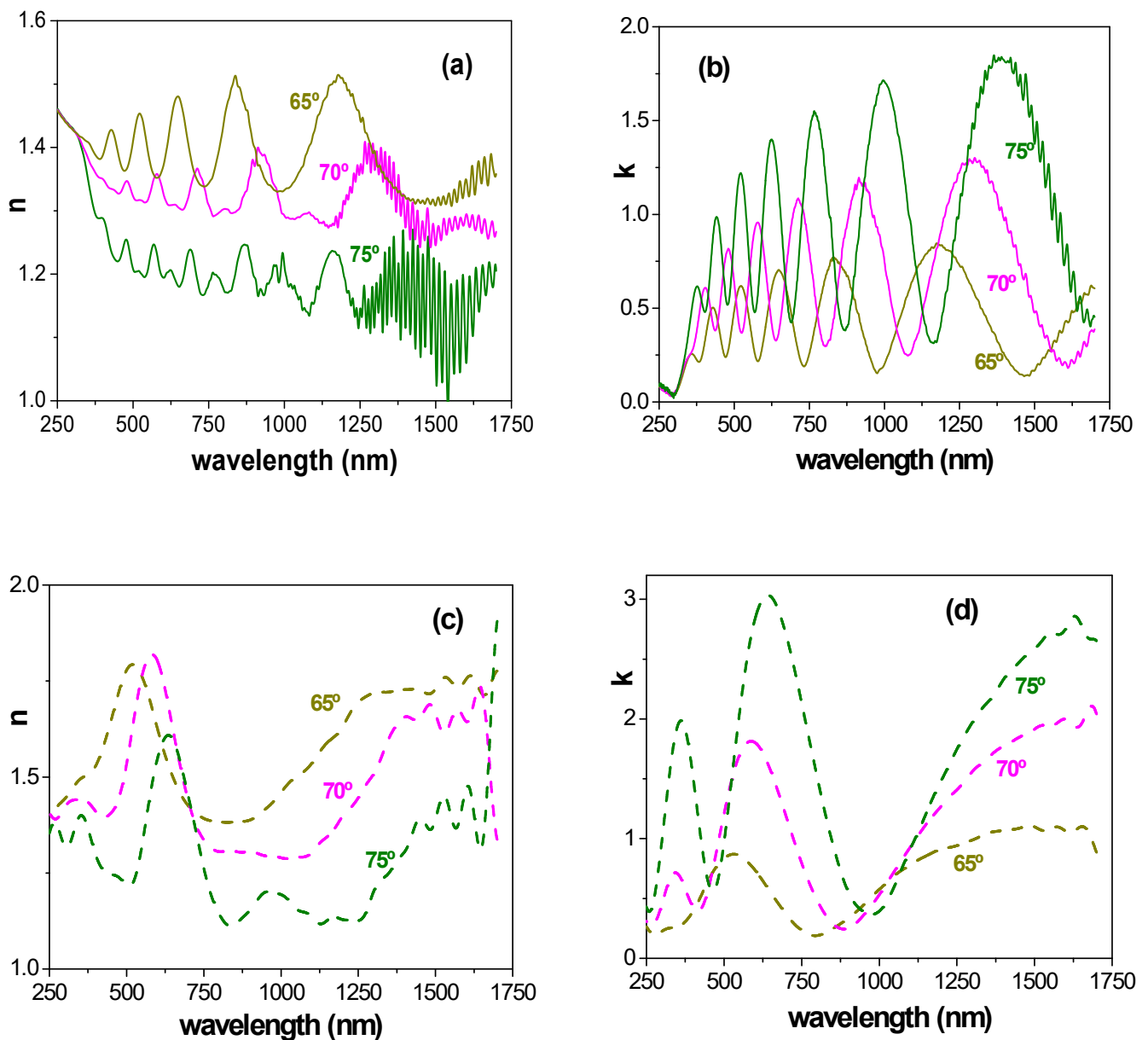


**Figure 4.** Wavelength dependence for the refractive index ( $n$ ) and the extinction coefficient ( $k$ ) at the three light incident angles: 65° (dark yellow lines), 70° (magenta lines), and 75° (green lines). (a,c): refractive index; (b,d): extinction coefficient. Solid lines: Ox(A)/SiO<sub>2</sub> sample; dashed lines: Ox(B)/SiO<sub>2</sub> sample.

The effect of sample geometry on  $n$  and  $k$  values can be more clearly observed in Figure 5, where a comparison of the wavelength dependence of both parameters for Ox(A)/SiO<sub>2</sub> and Ox(B)/SiO<sub>2</sub> samples at a light incident angle of 65° is presented and clear differences in both curve shape and values can be observed. Dark yellow horizontal dashed lines in Figure 5 indicate average values for each sample and parameter, with both the  $n$

and  $k$  values determined for the Ox(B)/SiO<sub>2</sub> sample being higher than those obtained for the Ox(A)/SiO<sub>2</sub>, but the black horizontal dashed-dot line in Figure 5a corresponds to the tabulated value (at 632.8 nm) of SiO<sub>2</sub> refractive index [66]. Moreover, since the dielectric constant is related to  $n$  and  $k$ :  $\varepsilon = (n + i \cdot k)^2$ , the wavelength dependence of  $\varepsilon_r$  and  $\varepsilon_i$  can also be determined, and they are shown as Supplementary Information (Figure S3).

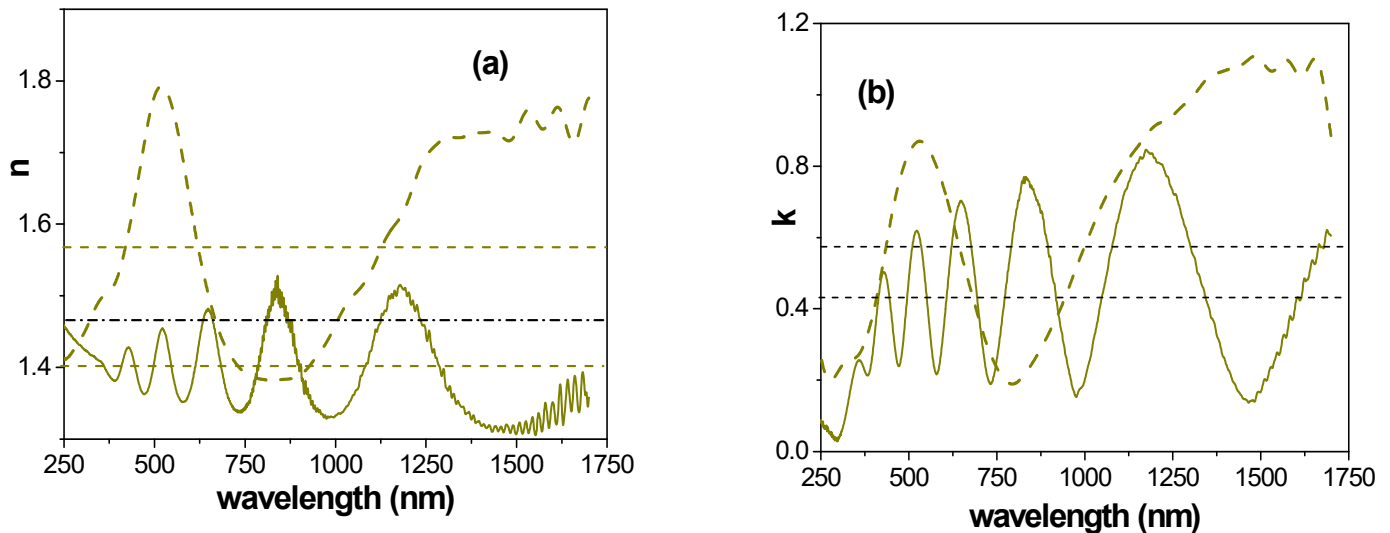


**Figure 5.** Comparison of wavelength dependence for the refractive index (a) and the extinction coefficient (b) at a light incident angle of 65°. Solid lines: Ox(A)/SiO<sub>2</sub> sample; dashed lines: Ox(b)/SiO<sub>2</sub> sample. Dark yellow horizontal lines indicate the average ( $\langle n \rangle$  and  $\langle k \rangle$ ) values for each sample; a black horizontal dashed-dot line indicates the tabulated value of SiO<sub>2</sub> refractive index (at  $\lambda = 632.8$  nm).

The effect of cover-layer material for samples with similar geometrical parameters was also considered by comparing the wavelength dependence of  $n$  and  $k$  values determined for the Ox(A)/SiO<sub>2</sub> sample with those obtained for the Ox(A) alumina support coated by ALD with a TiO<sub>2</sub> or a Fe<sub>2</sub>O<sub>3</sub> layer (Ox(A)/TiO<sub>2</sub> or Ox(A)/Fe<sub>2</sub>O<sub>3</sub> samples), and the obtained results are shown in Figure 6a,b for the Ox(A)/TiO<sub>2</sub> sample and Figure 6c,d for the Ox(A)/Fe<sub>2</sub>O<sub>3</sub>. As expected, differences in the values of the refractive index and extinction coefficient depending on the ceramic oxide coating layer were obtained, but also in the shape of the wavelength dependence, reducing significantly for both materials the oscillatory character of the refractive index as well as the effect of the incident angle.

A comparison of wavelength dependence (400–1700 nm interval) for  $n$  and  $k$  values determined at 65° for Ox(A)/SiO<sub>2</sub>, Ox(A)/TiO<sub>2</sub>, and Ox(A)/Fe<sub>2</sub>O<sub>3</sub> samples is presented in Figure 7, and from these results the following average values for both parameters (horizontal dashed lines in Figure 7) were obtained:  $\langle n(\text{Ox(A)/SiO}_2) \rangle = 1.40$ ;  $\langle n(\text{Ox(A)/TiO}_2) \rangle = 1.67$ ;  $\langle n(\text{Ox(A)/Fe}_2\text{O}_3) \rangle = 1.66$ ;  $\langle k(\text{Ox(A)/SiO}_2) \rangle = 0.47$ ;  $\langle k(\text{Ox(A)/TiO}_2) \rangle = 0.33$ ; and  $\langle k(\text{Ox(A)/Fe}_2\text{O}_3) \rangle = 0.24$ . Taking into account the similarity in geometrical parameters of these samples, modifications for different optical parameters ( $n$ ,  $k$ , as well as band gap, as determined by light transmission measurements [40]) are associated with the cover layer.



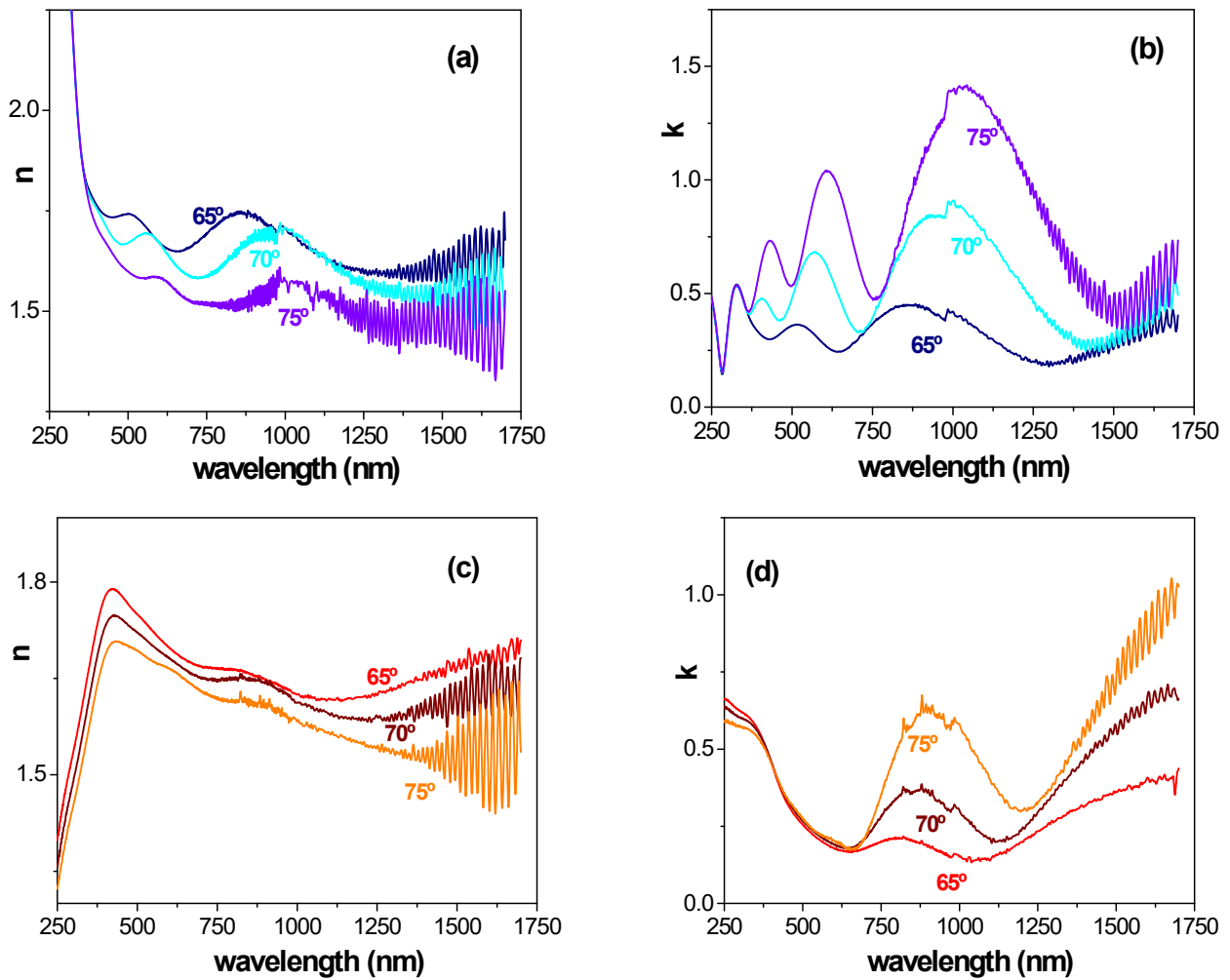


**Figure 6.** Effect of an Ox(A) support coated layer on refractive index (n) and extinction coefficient (k) for wavelengths ranging between 250 nm and 1700 nm determined at three different light incident angles. (a,b): Ox(A)/TiO<sub>2</sub> sample; (c,d): Ox(A)/Fe<sub>2</sub>O<sub>3</sub> sample.

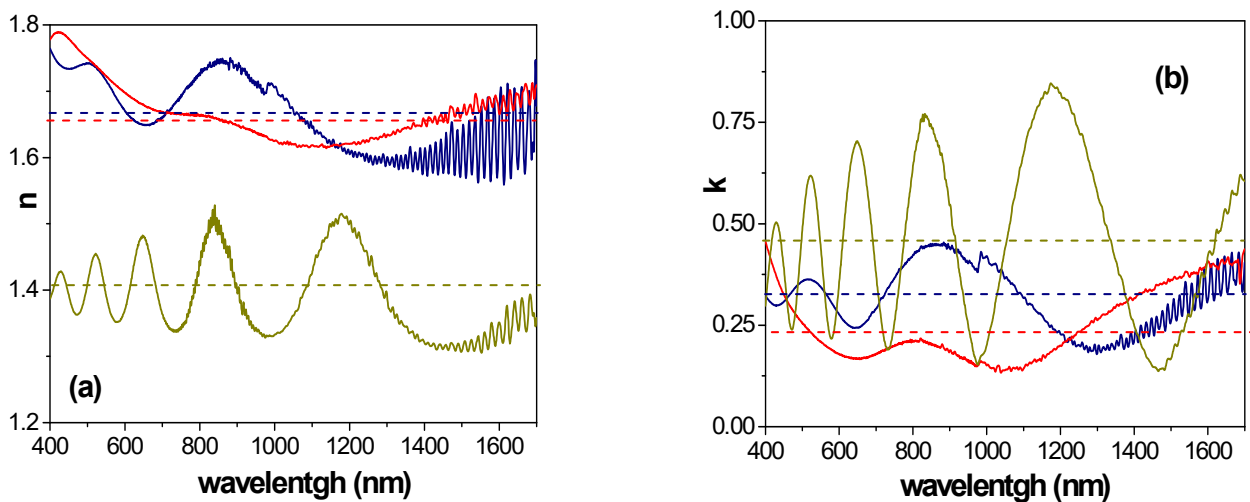


**Figure 7.** Comparison of wavelength dependence for the refraction index (a) and the extinction coefficient (b) at a light incident angle of 65° for the Ox(A)/SiO<sub>2</sub> sample (dark yellow line), the Ox(A)/TiO<sub>2</sub> sample (blue line), and the Ox(A)/Fe<sub>2</sub>O<sub>3</sub> sample (red line). Horizontal dashed lines indicate average  $\langle n \rangle$  or  $\langle k \rangle$  values for each sample.

As it was already indicated, a particular property of nanoporous alumina structures (NPASs) obtained by the electrochemical anodization method is photoluminescence (PL), which was initially reported in the 1980s and is ascribed to structural defects, namely oxygen vacancies, present in NPASs as a consequence of the incorporation of impurities during the anodic oxidation process [35]. Since PL can be of interest for different applications, a number of papers correlating PL spectra with sample fabrication parameters (mainly anodization voltage but also electrolyte solutions and electrolyte mixtures or temperature, which affects sample nanometric geometry) or even aluminum purity have been reported lately [67–71]. These results show PL curves with similar shapes and maximum intensity wavelengths ranging between 420 nm and 460 nm, depending on anodization voltage values using oxalic acid as the electrolyte (for excitation wavelengths around 330 nm). However, in the case of malonic acid, different curve shapes and maximum intensity wavelength values (between 450 nm and 520 nm) were obtained, whereas aluminum impurity only seems to reduce the intensity of the curves. Consequently, the photoluminescence character of the NPA-bSs and the possible effect of sample geometry and even cover layer material on PL results have also been considered. In fact, photoluminescence for different kinds of SiO<sub>2</sub>-based films (nanotextured SiO<sub>2</sub> and silicon oxynitride films, SiO<sub>2</sub>-coated ZnO nanoparticles, or SiO<sub>2</sub> layers on Si support) as well as for a layered nanostructure (multi-walled carbon nanotube-TiO<sub>2</sub> nanofiber composite), as a result of surface oxygen vacancies and other defects, have also been reported [71–77]. Therefore, an additional method to tune the intensity of PL is the use of appropriate coatings, which can have an active or passive role in PL effects.

Figure 8a shows a comparison of the photoluminescence spectra obtained for Ox(A)/SiO<sub>2</sub> and Ox(B)/SiO<sub>2</sub> samples using an excitation wavelength of 330 nm, and, as can be observed, the increase in sample pore-size/porosity does not modify the shape of the curve, with a maximum at a wavelength around 460 nm. In fact, the shape of the curves is similar to that obtained for SiO<sub>2</sub>-Si structures excited at 350 nm [76], as well as for high-purity alumina films (also obtained with 0.3 oxalic acid and deposited on soda-lime glass substrates [75]), when excited at 320 nm or 330 nm, but in that case the maximum intensity was at a wavelength of 400 nm or 410 nm. Moreover, the effect of coating-layer material on the photoluminescence spectrum for the NPA-bSs with similar geometry but different coating layers (SiO<sub>2</sub>, TiO<sub>2</sub>, or Fe<sub>2</sub>O<sub>3</sub>) is shown in Figure 8b, where the most significant difference is the intensity of the PL spectra depending on the cover layer material, with the following tendency: Ox/SiO<sub>2</sub> >> Ox/Fe<sub>2</sub>O<sub>3</sub> > Ox/TiO<sub>2</sub>, which indicates that both Fe<sub>2</sub>O<sub>3</sub> and TiO<sub>2</sub> have a passivating effect, thus substantially decreasing PL effects. These results support the possible use of the studied samples in bio-imaging, diagnostics, and sensing devices.

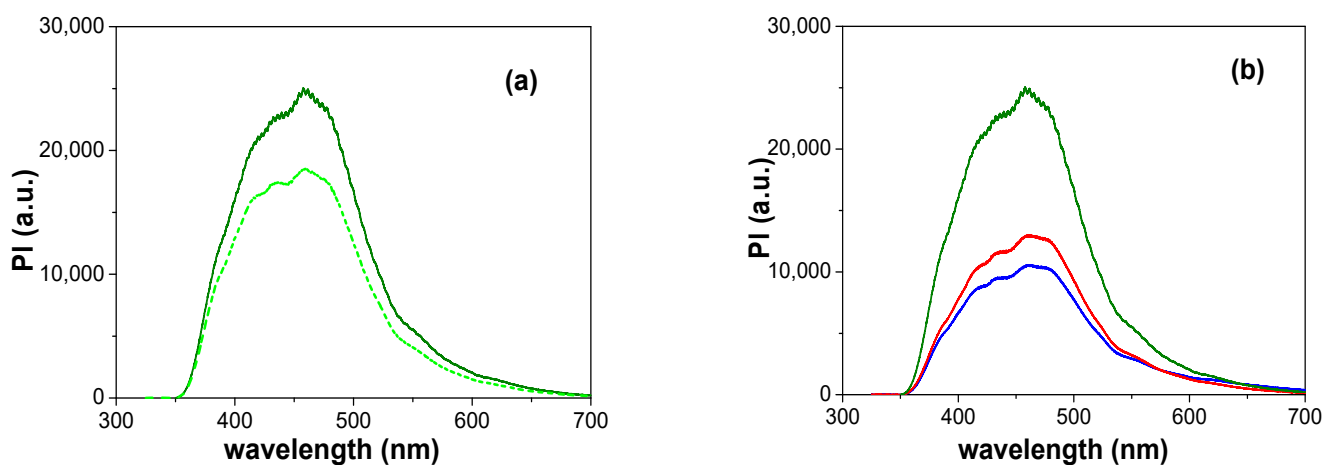


**Figure 8.** Photoluminescence spectra obtained for: (a) the Ox(A)/SiO<sub>2</sub> sample (solid line) and the Ox(B)/SiO<sub>2</sub> sample (dashed line); (b) the Ox(A)/SiO<sub>2</sub> sample (green line), the Ox(A)/TiO<sub>2</sub> sample (blue line), and the Ox(A)/Fe<sub>2</sub>O<sub>3</sub> sample (red line).

#### 4. Conclusions

The optical characterization of nanoporous alumina structures coated with different ceramic oxides by ALD technique, performed in this study by spectroscopy, ellipsometry, and photoluminescence measurements, clearly shows the influence of sample geometry and coating material on the value of a characteristic optical parameter such as the refraction index of the samples as well as on its oscillatory behavior; both factors also seem to affect the photoluminescence behavior of the studied samples. Moreover, surface inhomogeneity and the presence of impurities associated with sample fabrication seem also to affect the values of optical parameters, according to the SE results obtained at different light incidence angles. On the other hand, this analysis indirectly supports the suitability of the ALD technique for functional modification of nanoporous structures, showing the potential application of these NPA-bSs platforms to nanophotonics, optical sensing, or biosensing.

**Supplementary Materials:** The following supporting information can be downloaded at: <https://www.mdpi.com/article/10.3390/mi14040839/s1>, Figure S1: Wavelength dependence for  $\tan(\Psi)$  and  $\cos(\Delta)$  at three light incident angles:  $65^\circ$  (dark yellow lines),  $70^\circ$  (magenta lines), and  $75^\circ$  (green lines) for sample Ox(B)/SiO<sub>2</sub>. Without applying data refinement (smoothing); Figure S2: Variation of atomic concentration percentages of the different elements detected on the Ox/SiO<sub>2</sub> sample surface with the XPS sputtering time; Figure S3: Wavelength dependence of the dielectric constant (real part (a) and imaginary part (b)) for Ox(A)/SiO<sub>2</sub> sample (solid line) and Ox(B)/SiO<sub>2</sub> sample (dashed line) determined for a light incident angle of  $65^\circ$ .

**Author Contributions:** Synthesis of NPA-bSs, V.V. and A.S.G., under the supervision of V.M.P. and V.V.; sample electron microscopy analysis, V.V.; XPS and optical measurements A.L.C. and A.D., supervised by J.B.; conceptualization, design, and discussion of the experiments, V.M.P. and J.B. All authors contributed to the co-writing of the manuscript. All authors have read and agreed to the published version of the manuscript.

**Funding:** This research was funded by the Spanish MCI under grant number PID2019-108075RB-C32/AEI/10.13039/501100011033.

**Data Availability Statement:** Not applicable.

**Acknowledgments:** M. V. Martinez de Yuso, from the Central Research Services of Malaga University, is acknowledged for XPS measurements. The scientific support of the Laboratory of Nanoporous Membranes and facilities from the SCTs of the University of Oviedo are also gratefully recognized.

**Conflicts of Interest:** The authors declare no conflict of interest.

#### References

1. Testoni, G.E.; Chiappim, W.; Pessoa, R.S.; Fraga, M.A.; Miyakawa, W.; Sakane, K.K.; Galvão, N.K.A.M.; Vieira, L.; Maciel, H.S. Influence of the Al<sub>2</sub>O<sub>3</sub> partial-monolayer number on the crystallization mechanism of TiO<sub>2</sub> in ALD TiO<sub>2</sub>/Al<sub>2</sub>O<sub>3</sub> nanolaminates and its impact on the material properties. *J. Phys. D Appl. Phys.* **2016**, *49*, 375301. [CrossRef]
2. Chiappim, W.; Testoni, G.; Miranda, F.; Fraga, M.; Furlan, H.; Saravia, D.A.; Sobrinho, A.d.S.; Petraconi, G.; Maciel, H.; Pessoa, R. Effect of Plasma-Enhanced Atomic Layer Deposition on Oxygen Overabundance and Its Influence on the Morphological, Optical, Structural, and Mechanical Properties of Al-Doped TiO<sub>2</sub> Coating. *Micromachines* **2021**, *12*, 588. [CrossRef]
3. Rahman, M.M.; Kim, J.-G.; Kim, D.-H.; Kim, T.-W. Characterization of Al Incorporation into HfO<sub>2</sub> Dielectric by Atomic Layer Deposition. *Micromachines* **2019**, *10*, 361. [CrossRef] [PubMed]
4. Mackus, A.J.M.; Schneider, J.R.; MacIsaac, C.; Baker, J.G.; Bent, S.F. Synthesis of Doped, Ternary, and Quaternary Materials by Atomic Layer Deposition: A Review. *Chem. Mater.* **2019**, *31*, 1142–1183. [CrossRef]
5. Oviroh, P.O.; Akbarzadeh, R.; Pan, D.; Coetzee, R.A.M.; Jen, T.C. New development of atomic layer deposition: Processes, methods and applications. *Sci. Technol. Adv. Mater.* **2019**, *20*, 465–496. [CrossRef] [PubMed]
6. Geng, G.; Zhang, Z.; Li, C.; Pan, R.; Li, Y.; Yang, H.; Li, J. Atomic Layer Assembly Based on Sacrificial Templates for 3D Nanofabrication. *Micromachines* **2022**, *13*, 856. [CrossRef] [PubMed]
7. Shkondin, E.; Takayama, O.; Panah, M.E.A.; Liu, P.; Larsen, P.V.; Mar, M.D.; Jensen, F.; Lavrinenko, A.V. Large-scale high aspect ratio Al-doped ZnO nanopillars arrays as anisotropic metamaterials. *Opt. Mater. Express* **2017**, *7*, 1606–1627. [CrossRef]
8. Shkondin, E.; Takayama, O.; Lindhard, J.M.; Larsen, P.V.; Mar, M.D.; Jensen, F.; Lavrinenko, A.V. Fabrication of high aspect ratio TiO<sub>2</sub> and Al<sub>2</sub>O<sub>3</sub> nanogratings by atomic layer deposition. *J. Vac. Sci. Technol. A Vac. Surf. Film.* **2016**, *34*, 031605. [CrossRef]

9. O'Neill, B.J.; Jackson, D.H.K.; Lee, J.; Canlas, C.; Stair, P.C.; Marshall, C.L.; Elam, J.W.; Kuech, T.F.; Dumesic, J.A.; Huber, J.W. Catalyst Design with Atomic Layer Deposition. *ACS Catal.* **2015**, *5*, 1804–1825. [[CrossRef](#)]
10. Zhang, B.; Qin, Y. Interface Tailoring of Heterogeneous Catalysts by Atomic Layer Deposition. *ACS Catal.* **2018**, *8*, 10064–10081. [[CrossRef](#)]
11. Ivanova, T.V.; Homola, T.; Bryukvin, A.; Cameron, D.C. Catalytic Performance of Ag<sub>2</sub>O and Ag Doped CeO<sub>2</sub> Prepared by Atomic Layer Deposition for Diesel Soot Oxidation. *Coatings* **2018**, *8*, 237. [[CrossRef](#)]
12. Chen, X.; Baumgart, H. Advances in Atomic Layer Deposition (ALD) Nanolaminate Synthesis of Thermoelectric Films in Porous Templates for Improved Seebeck Coefficient. *Materials* **2020**, *13*, 1283. [[CrossRef](#)] [[PubMed](#)]
13. Koshtyal, Y.; Nazarov, D.; Ezhov, I.; Mitrofanov, I.; Kim, A.; Rymyantsev, A.; Lyutakov, O.; Popovich, A.; Maximov, M. Atomic Layer Deposition of NiO to Produce Active Material for Thin-Film Lithium-Ion Batteries. *Coatings* **2019**, *9*, 301. [[CrossRef](#)]
14. Wen, L.; Zhou, M.; Wang, C.; Mi, Y.; Lei, Y. Nanoengineering Energy Conversion and Storage Devices via Atomic Layer Deposition. *Adv. Energy Mater.* **2016**, *6*, 1600468. [[CrossRef](#)]
15. Mäntymäki, M.; Ritala, M.; Leskelä, M. Metal Fluorides as Lithium-Ion Battery Materials: An Atomic Layer Deposition Perspective. *Coatings* **2018**, *8*, 277. [[CrossRef](#)]
16. Seppänen, H.; Kim, I.; Etula, J.; Ubyivovk, E.; Bouravleuv, A.; Lipsanen, H. Aluminum Nitride Transition Layer for Power Electronics Applications Grown by Plasma-Enhanced Atomic Layer Deposition. *Materials* **2019**, *12*, 406. [[CrossRef](#)] [[PubMed](#)]
17. Kim, W.; Yasmeen, S.; Nguyen, C.T.; Lee, H.-B.-R.; Choi, D. Toward Enhanced Humidity Stability of Triboelectric Mechanical Sensors via Atomic Layer Deposition. *Nanomaterials* **2021**, *11*, 1795. [[CrossRef](#)]
18. Wilson, R.L.; Simion, C.E.; Blackman, C.S.; Carmalt, C.J.; Stanoiu, A.; Di Maggio, F.; Covington, J.A. The Effect of Film Thickness on the Gas Sensing Properties of Ultra-Thin TiO<sub>2</sub> Films Deposited by Atomic Layer Deposition. *Sensors* **2018**, *18*, 735. [[CrossRef](#)]
19. Xu, H.; Akbari, M.K.; Kumar, S.; Verpoort, F.; Zhuiykov, S. Atomic layer deposition—State-of-the-art approach to nanoscale hetero-interfacial engineering of chemical sensors electrodes: A review. *Sens. Actuators B Chem.* **2021**, *331*, 129403. [[CrossRef](#)]
20. Huang, J.; Wang, X.; Wang, Z.L. Controlled Replication of Butterfly Wings for Achieving Tunable Photonic Properties. *Nano Lett.* **2006**, *6*, 2325–2331. [[CrossRef](#)]
21. Masuda, H.; Fukuda, K. Ordered Metal Nanohole Arrays Made by a Two-Step Replication of Honeycomb Structures of Anodic Alumina. *Science* **1995**, *268*, 1466–1468. [[CrossRef](#)] [[PubMed](#)]
22. Nielsch, K.; Choi, J.; Schwirn, K.; Wehrspohn, R.B.; Gösele, U. Self-ordering regimes of porous alumina: The 10% porosity rule. *Nano Lett.* **2002**, *2*, 677–680. [[CrossRef](#)]
23. Kennard, R.; DeSisto, W.J.; Mason, M.D. Molecular diffusivity measurement through an alumina membrane using time-resolved fluorescence imaging. *Appl. Physics Lett.* **2010**, *97*, 213701. [[CrossRef](#)]
24. Vázquez, M.I.; Romero, V.; Vega, V.; García, J.; Prida, V.M.; Hernado, B.; Benavente, J. Morphological, Chemical Surface, and Diffusive Transport Characterizations of a Nanoporous Alumina Membrane. *Nanomaterials* **2015**, *5*, 2192–2202. [[CrossRef](#)]
25. Martín, R.; Manzano, C.V.; Martín-González, M. In-depth study of self-ordered porous alumina in the 140–400 nm pore diameter range. *Micropor. Mesopor. Mat.* **2012**, *151*, 311–316. [[CrossRef](#)]
26. Ruiz-Clavijo, A.; Caballero-Calero, O.; Martín-González, M. Revisiting anodic alumina templates: From fabrication to applications. *Nanoscale* **2021**, *13*, 2227–2265. [[CrossRef](#)]
27. Prida, V.M.; Sanz, R.; Vega, V.; Navas, D.; Pirota, K.R.; Asenjo, A.; Hernández-Vélez, M.; Hernando, B.; Vázquez, M. Title. *Encycl. Nanosci. Nanotechnol.* **2011**, *22*, 509–532.
28. Proenca, M.P.; Sousa, C.T.; Ventura, J.; Araújo, J.P. *Cylindrical Magnetic Nanotubes: Synthesis, Magnetism and Applications in Magnetic Nano- and Microwires: Design, Synthesis, Properties and Applications*, 2nd ed.; Vázquez, M., Ed.; Woodhead Publishing Series in Electronic and Optical Materials; Elsevier: Amsterdam, The Netherlands, 2020; ISBN 978-0-08-102832-2.
29. Bluhm, E.A.; Schroeder, N.C.; Bauer, E.; Fife, J.N.; Chamberlin, R.M.K.; Abney, D.; Young, J.S.; Jarvinen, G.D. Surface Effects on Metal Ion Transport across Porous Alumina Membranes. 2. Trivalent Cations: Am, Tb, Eu, and Fe. *Langmuir* **2000**, *16*, 7056–7060. [[CrossRef](#)]
30. Aw, M.S.; Bariana, M.; Losic, D. Nanoporous Anodic Alumina for Drug Delivery and Biomedical Applications. In *Nanoporous Alumina*; Losic, D., Santos, A., Eds.; Materials Science Series; Springer: Cham, Switzerland, 2015; Volume 219. [[CrossRef](#)]
31. Davoodi, E.; Zhianmanesh, M.; Montazerian, H.; Milani, A.S.; Hoorfar, M. Nano-porous anodic alumina: Fundamentals and applications in tissue engineering. *J. Mater. Sci. Mater. Med.* **2021**, *31*, 60. [[CrossRef](#)]
32. Kumeria, T.; Santos, A.; Losic, D. Nanoporous Anodic Alumina Platforms: Engineered Surface Chemistry and Structure for Optical Sensing Applications. *Sensors* **2014**, *14*, 11878–11918. [[CrossRef](#)]
33. Law, C.S.; Lim, S.Y.; Abell, A.D.; Voelcker, N.H.; Santos, A. Nanoporous Anodic Alumina Photonic Crystals for Optical Chemo- and Biosensing: Fundamentals, Advances, and Perspectives. *Nanomaterials* **2018**, *8*, 788. [[CrossRef](#)] [[PubMed](#)]
34. Cuevas, A.L.; González, A.S.; Vega, V.; Prida, V.M.; Benavente, J. Optical and Electrochemical Characterization of Nanoporous Alumina Structures: Pore Size, Porosity, and Structure Effect. *Appl. Sci.* **2020**, *10*, 4864. [[CrossRef](#)]
35. Yamamoto, Y.; Baba, N.; Tajima, S. Coloured materials and photoluminescence centres in anodic film of aluminium. *Nature* **1981**, *289*, 572–574. [[CrossRef](#)]
36. Du, Y.; Cai, W.L.; Mo, C.M.; Chen, J. Preparation and photoluminescence of alumina membranes with ordered pore arrays. *Appl. Phys. Lett.* **1999**, *74*, 2951–2953. [[CrossRef](#)]

37. Peng, H.J.; Ho, Y.L.; Yu, X.J.; Kwok, H.S. Enhanced coupling of light from organic light emitting diodes using nanoporous films. *J. Appl. Phys.* **2004**, *96*, 1649. [[CrossRef](#)]
38. Moghadam, H.; Samini, A.; Behzadmer, A. Effect of nanoporous anodic aluminium oxide (AAO) characteristics on solar absorptivity. *Trans. Phenom. Nano Micro Scales* **2013**, *1*, 110–116.
39. Romero, V.; Vega, V.; García, J.; Zierold, R.; Nielsch, K.; Prida, V.M.; Hernando, B.; Benavente, J. Changes in morphology and ionic transport induced by ALD SiO<sub>2</sub> coating of nanoporous alumina membranes. *ACS Appl. Mater. Interfaces* **2013**, *5*, 3556–3564. [[CrossRef](#)]
40. Cuevas, A.L.; Martínez de Yuso, M.V.; Vega, V.; González, A.S.; Prida, V.M.; Benavente, J. Influence of ALD Coating Layers on the Optical Properties of Nanoporous Alumina-Based Structures. *Coatings* **2019**, *9*, 43. [[CrossRef](#)]
41. Cuevas, A.L.; Martínez de Yuso, M.V.; Gelde, L.; González, A.S.; Vega, V.; Cuevas, A.L.; Prida, V.M.; Benavente, J. Chemical, optical and transport characterization of ALD modified nanoporous alumina based structures. *J. Ind. Eng. Chem.* **2020**, *91*, 139–148. [[CrossRef](#)]
42. Richey, N.E.; de Paula, C.; Bent, F.S. Understanding chemical and physical mechanisms in atomic layer deposition. *J. Chem. Phys.* **2020**, *152*, 040902. [[CrossRef](#)]
43. Santos, A.; Alba, M.; Rahman, M.M.; Formentín, P.; Ferré-Borrull, J.; Pallarés, J. Structural tuning of photoluminescence in nanoporous anodic alumina by hard anodization in oxalic and malonic acids. *Nanoscale Res. Lett.* **2012**, *7*, 22. [[CrossRef](#)]
44. Villalobos-Mendoza, B.; Granados-Agustín, F.S.; Aguirre-Aguirre, D.; Cornejo-Rodríguez, A. Phase shifting interferometry using a spatial light modulator to measure optical thin films. *Appl. Opt.* **2015**, *54*, 7997–8003. [[CrossRef](#)] [[PubMed](#)]
45. Ghim, Y.S.; Rhee, H.G. Instantaneous thickness measurement of multilayer films by single-shot angle-resolved spectral reflectometry. *Opt. Lett.* **2019**, *44*, 5418–5421. [[CrossRef](#)] [[PubMed](#)]
46. Algarra, M.; Cuevas, A.L.; Martínez de Yuso, M.V.; Benavente, J. Insights into the formation of an emissive CdTe-quantum-dots/cellulose hybrid film. *J. Colloid Interface Sci.* **2020**, *579*, 722–774. [[CrossRef](#)] [[PubMed](#)]
47. Papadimitriou, D.N. Engineering of optical and electrical properties of electrodeposited highly doped Al:ZnO and In:ZnO for cost-effective photovoltaic devices technology. *Micromachines* **2022**, *13*, 1966. [[CrossRef](#)] [[PubMed](#)]
48. Hilfiker, J.N.; Pietz, B.; Dodge, B.; Sun, J.; Hong, N.; Schoeche, S. Spectroscopic ellipsometry characterization of coatings on biaxially anisotropic polymeric substrates. *Appl. Surf. Sci.* **2017**, *421*, 500–507. [[CrossRef](#)]
49. Kamble, S.; Patil, S.; Kulkarni, M.; Murthy, A.V.R. Spectroscopic Ellipsometry of fluid and gel phase lipid bilayers in hydrated conditions. *Coll. Surf. B Biointerf.* **2019**, *179*, 55–61. [[CrossRef](#)]
50. Pizarda, M.; Altinas, Z. Recent progress in optical sensors for biomedical diagnosis. *Micromachines* **2020**, *11*, 356. [[CrossRef](#)]
51. Losurdo, M.; Begmair, M.; Bruno, G.; Cattelan, D.; Cobet, C.; De Martina, A.; Fleischer, K.; Dohcevic-Mitrovic, Z.; Esser, N.; Galliet, M.; et al. Spectroscopic ellipsometry and polarimetry for materials and systems analysis at the nanoscale: State-of-art, potential, and perspectives. *J. Nanopart. Res.* **2009**, *11*, 1521–1554. [[CrossRef](#)]
52. Li, L.; Lei, J.; Wu, L.; Pan, F. *Spectroscopic Ellipsometry in Handbook of Modern Coating Technologies: Advanced Characterization Methods*; Elsevier: Amsterdam, The Netherlands, 2021; pp. 45–83.
53. Bachmann, J.; Zierold, R.; Chong, Y.T.; Hauert, R.; Sturm, C.; Schmidt-Grund, R.; Rheinländer, B.; Grundmann, M.; Gösele, U.; Nielsch, K. A Practical, Self-Catalytic, Atomic Layer Deposition of Silicon Dioxide. *Angew. Chem. Int. Ed.* **2008**, *47*, 6177–6179. [[CrossRef](#)]
54. Gautam, L.K.; Junda, M.M.; Haneef, H.F.; Collins, R.W.; Nikolas, J.; Podraza, N.J. Spectroscopic Ellipsometry Studies of n-i-p Hydrogenated Amorphous Silicon Based Photovoltaic Devices. *Materials* **2016**, *9*, 128. [[CrossRef](#)] [[PubMed](#)]
55. González, A.S.; Vega, V.; Cuevas, A.L.; Martínez de Yuso, M.V.; Prida, V.M.; Benavente, J. Surface Modification of Nanoporous Anodic Alumina during Self-Catalytic Atomic Layer Deposition of Silicon Dioxide from (3-Aminopropyl)Triethoxysilane. *Materials* **2021**, *14*, 5052. [[CrossRef](#)]
56. Lee, W.; Park, S.-J. Porous Anodic Aluminum Oxide: Anodization and Templated Synthesis of Functional Nanostructures. *Chem. Rev.* **2014**, *114*, 7487–7556. [[CrossRef](#)] [[PubMed](#)]
57. Weber, M.; Julbe, A.; Ayrál, A.; Miele, P.; Bechelany, M. Atomic Layer Deposition for Membranes: Basics, Challenges, and Opportunities. *Chem. Mater.* **2018**, *30*, 7368–7390. [[CrossRef](#)]
58. Schneider, C.A.; Rasband, W.S.; Eliceiri, K.W. NIH Image to ImageJ: 25 years of image analysis. *Nat. Methods.* **2012**, *9*, 671–675. [[CrossRef](#)]
59. Gâlcă, A.C.; Kooij, E.S.; Wormeester, H.; Salm, C.; Leca, V.; Rector, J.H.; Poelsema, B. Structural and optical characterizations of porous anodic aluminium oxide. *J. Appl. Phys.* **2003**, *94*, 4296–4305. [[CrossRef](#)]
60. Logothetidis, S.; Gioti, M.; Gravalidis, C. Optical and electronic characterization on polymeric membranes. *Synth. Met.* **2003**, *138*, 369–374. [[CrossRef](#)]
61. Tompkins, G.; Hilfiker, J.N. *Spectroscopic Ellipsometry: Practical Application to Thin Film Characterization*, 1st ed.; Momentum Press: New York, NY, USA, 2016; pp. 57–70.
62. Algarra, M.; Ana, L.; Cuevas, A.L.; Martínez de Yuso, M.V.; Romero, R.; Alonso, B.; Casado, C.M.; Benavente, J. Optical and Physicochemical Characterizations of a Cellulosic/CdSe-QDs@S-DAB5 Film. *Nanomaterials* **2022**, *12*, 484. [[CrossRef](#)]
63. Zheng, H.; Zhang, R.-J.; Li, D.-H.; Chen, X.; Wang, S.-Y.; Zheng, Y.-X.; Li, M.-J.; Hu, Z.-G.; Dai, N.; Chen, L.-Y. Optical properties of Al-doped ZnO films in the infrared region and their adsorption applications. *Nanoscale Res. Lett.* **2018**, *13*, 149. [[CrossRef](#)]

64. Bao, Y.; Xu, S. Variable-period oscillations in optical spectra in sub-bandgap long wavelength region: Signatures of new dispersion of refractive index? *J. Phys. D Appl. Phys.* **2021**, *54*, 155102. [[CrossRef](#)]
65. Yamaguchi, S.; Sugimoto, Y.; Fujiwara, H. Characterization of textured SnO<sub>2</sub>:F layers by ellipsometry using glass-side illumination. *Thin Solid Films* **2013**, *534*, 149–154. [[CrossRef](#)]
66. Vaxa Software. Available online: [www.vaxasoftware.com](http://www.vaxasoftware.com) (accessed on 1 March 2023).
67. Chung, C.K.; Chu, B.Y.; Tsai, C.H.; Hsu, C.R. Photoluminescence enhancement of nanoporous alumina using one-step anodization of high- and low-purity aluminium at room temperature. *Mater. Lett.* **2017**, *190*, 157–160. [[CrossRef](#)]
68. Reddy, P.R.; Ajith, K.; Udayashankar, N. Morphology and photoluminescence of nano-porous anodic alumina membranes obtained in oxalic acid at different anodization potentials. *Nano Express* **2020**, *1*, 010047. [[CrossRef](#)]
69. Vrublevsky, I.A.; Chernyakova, K.V.; EMuratova, E.N.; Spivak, Y.M.; Moshnikov, V.A. Photoluminescence and its damping kinetics of nanoporous alumina membranes formed in solutions of various carboxylic acids. *Mater. Sci. Semicond. Process.* **2020**, *106*, 104755. [[CrossRef](#)]
70. Acosta, L.K.; Law, C.S.; Santos, A.; Ferré-Borrull, J.; Marsal, L.F. Tuning intrinsic photoluminescence from light-emitting multispectral nanoporous anodic alumina photonic crystals. *APL Photonics* **2022**, *7*, 026108. [[CrossRef](#)]
71. Choudhari, K.S.; Kulkarni, S.D.; Unnikrishnan, V.K.; Sinha, R.K.; Santhosh, C.; George, S.D. Optical characterizations of nanoporous anodic alumina for thickness measurements using interference oscillations. *Nano Struct. Nano Objects* **2019**, *19*, 100354. [[CrossRef](#)]
72. Pirouz, A.; Ebrahimi, A.; Karbassian, F.; Mahajerzadeh, S. Photoluminescence from SiO<sub>2</sub> nanostructures prepared by a sequential RIE process. In Proceedings of the IEEE Nanotechnology Materials & Devices Conference, Jeju, Republic of Korea, 18–21 October 2011; pp. 372–375. [[CrossRef](#)]
73. Kumar, K.; Poulouse, V.; Laz, Y.T.; Chandra, F.; Abubakar, S.; Abdelhamid, A.S.; Alzamly, A.; Saleh, N. Temperature Control of Yellow Photoluminescence from SiO<sub>2</sub>-Coated ZnO Nanocrystals. *Nanomaterials* **2022**, *12*, 3368. [[CrossRef](#)]
74. Shi, Y.; He, L.; Guang, F.; Li, L.; Xin, Z.; Liu, R. A Review: Preparation, Performance, and Applications of Silicon Oxynitride Film. *Micromachines* **2019**, *10*, 552. [[CrossRef](#)]
75. Valeev, R.G.; Petukhov, D.I.; Kriventsov, V.V. Structure and optical properties of thin porous anodic alumina films synthesized on a glass surface. *Phys. Procedia* **2016**, *84*, 415–420. [[CrossRef](#)]
76. Baraban, A.P.; Samarin, S.N.; Prokofiev, V.A.; Dmitriev, V.A.; Selivanov, A.A.; Petrov, Y. Luminescence of SiO<sub>2</sub> layers on silicon at various types of excitation. *J. Luminisc.* **2019**, *205*, 102–108. [[CrossRef](#)]
77. Chetibi, L.; Busko, T.; Kulish, N.P.; Hamana, D.; Chaieb, S.; Achour, S. Photoluminescence properties of TiO<sub>2</sub> nanofibers. *J. Nanopart. Res* **2017**, *19*, 129. [[CrossRef](#)]

**Disclaimer/Publisher's Note:** The statements, opinions and data contained in all publications are solely those of the individual author(s) and contributor(s) and not of MDPI and/or the editor(s). MDPI and/or the editor(s) disclaim responsibility for any injury to people or property resulting from any ideas, methods, instructions or products referred to in the content.